11-1-2023

Experimental study of topology optimized, additively manufactured microchannel heat sinks designed using a homogenization approach

S. Ozguc
Purdue University

T F.G. Teague

L. Pan

Justin Weibel
jaweibel@purdue.edu

Ozguc, S.; Teague, T F.G.; Pan, L.; and Weibel, Justin, "Experimental study of topology optimized, additively manufactured microchannel heat sinks designed using a homogenization approach" (2023). *CTRC Research Publications.* Paper 406.
http://dx.doi.org/https://doi.org/10.1016/j.ijheatmasstransfer.2023.124108

International Journal of Heat and Mass Transfer 209 (2023) 124108

Contents lists available at ScienceDirect

International Journal of Heat and Mass Transfer

journal homepage: www.elsevier.com/locate/hmt

Experimental study of topology optimized, additively manufactured microchannel heat sinks designed using a homogenization approach

Serdar Ozguc, Trevor F.G. Teague, Liang Pan, Justin A. Weibel*

Cooling Technologies Research Center and School of Mechanical Engineering, Purdue University, 585 Purdue Mall, West Lafayette, IN, 47907

ARTICLE INFO

Article history:
Received 28 November 2022
Revised 23 January 2023
Accepted 15 March 2023
Available online 28 March 2023

Keywords:
Additive manufacturing
Microchannel
Heat sink
Topology optimization
Multi-objective optimization

ABSTRACT

Topology optimization generates complex geometry heat sink designs having intricate features well-suited for fabrication by additive manufacturing. In particular, a homogenization approach to topology optimization creates microchannel heat sink designs wherein the material porosity distribution corresponds to microstructures of varying dimensions, thereby eliminating the need to penalize the porosities to achieve binarized solid/liquid designs. This approach is inherently able to take into consideration the capabilities and limitations of available additive manufacturing processes as the types of microstructures can be user-defined. The current study is the first to fabricate and experimentally test microchannel heat sink designs that are topology optimized using the homogenization approach. To this end, a multi-objective optimization is performed to generate a series of Pareto optimal designs that minimize pressure drop and thermal resistance. The effect of the grid resolution is investigated. The resulting topology optimized designs are found to have different geometries and performances with different grid cell sizes because this impacts the physical dimensions of the microstructures. A series of pin fin arrays with different grid cell sizes and fin thicknesses are fabricated using Direct Metal Laser Sintering of AlSi10Mg. The additively manufactured surfaces have high roughness which creates connections between pin fins with small gap sizes and creates tortuous flow paths. The smallest pin fin that consistently survived the fabrication process is ~0.25 mm thick and hence series of topology optimized microchannel heat sinks with a 0.5 mm grid cell size are additively manufactured. The pressure drop and thermal resistance of the fabricated heat sinks are experimentally characterized, and the measured results lie on the Pareto optimality curve predicted by the topology optimization algorithm. This work demonstrates that the homogenization approach to topology optimization generates high-performance microchannel heat sink designs that can be achieved using available additive manufacturing processes.

1. Introduction

Heat sinks are commonly used in the thermal management of electronic and electromechanical devices to provide a low-thermal-resistance pathway between the heat generating components and the cooling fluid. Factors such as coolant type, boundary conditions, material properties, and performance objectives dictate the optimal heat sink geometry and dimensions. There have been many studies on the design, optimization, and testing of heat sink geometries to develop high-performance thermal management solutions for a wide array of applications. However, heat sink designs were limited by conventional fabrication methods for which simple geometries with better mass manufacturability were preferred over application-specific, optimized parts with intricate features. The emergence of commercial additive manufacturing (AM) processes that enable the fabrication of complex structures has created an increased interest in the design of heat sink geometries having lower thermal and flow resistances by leveraging this increased design freedom.

There have been many different heat sink designs proposed to improve heat dissipation performance. Some of these novel heat sinks are designed using engineering intuition where knowledge of fluid dynamics and heat transfer principles are used to propose geometries expected to improve the hydrodynamic and thermal performance. For example, Fasano et al. [1] proposed a novel air-cooled 'Pitot heat sink' design having a secondary flow path on top of the heat sink which connects to the main flow path between rectangular fins through the internal openings of the fins. This complex flow path, made possible by AM, was fabricated using direct metal laser sintering (DMLS) in AlSiMg and experiments showed up to 95% improvement in convective thermal transmittance compared to the benchmark. Kempers et al. [2] used a multi-metal electrodeposition AM process to design and fabricate

* Corresponding author.
E-mail address: jaweibel@purdue.edu (J.A. Weibel).

https://doi.org/10.1016/j.ijheatmasstransfer.2023.124108
0017-9310/

Nomenclature

A_b	heat sink base area, m^2
c_p	coolant specific heat capacity, J/kg-K
f_{cost}	cost function, -
H	fin/channel height, m
H_b	base thickness, m
k	coolant thermal conductivity, W/m-K
m	weighting factor, -
ΔP	pressure drop, Pa
ΔP_{exp}	experimentally measured pressure drop, Pa
$\bar{P}$	pressure normalization constant, Pa
Q	total heat input, W
Q_{loss}	parasitic heat losses, W
R	thermal resistance, K/W
R_w	weighted thermal resistance, K/W
$\bar{R}$	thermal resistance normalization constant, K/W
R_f	filter radius, m
R_{sh}	shunt resistor electrical resistance, Ω
R_{exp}	experimentally measured thermal resistance, K/W
T_b	base temperature, K
T_{exp}	experimentally measured base temperature, K
t	fin thickness, m
T_c	coolant temperature, K
$T_{c,in}$	inlet coolant temperature, K
T_{heater}	heater temperature, K
T_{max}	maximum base temperature, K
T_∞	ambient temperature, K
$\bar{v}$	velocity, m/s
$\dot{V}$	flow rate, m^3/s
V_h	heater voltage drop, V
V_{sh}	shunt resistor voltage drop, V
w_f	filter weight, -
w	channel width, m
x	grid cell position, m
Δx	grid cell size, m

Greek Symbols

ε	design variable, -
ε_f	filtered design variable, -
λ	thresholding thickness, m
μ	coolant dynamic viscosity, Pa-s
ρ	coolant density, kg/m^3

Acronyms

AM	additive manufacturing
DMLS	direct metal laser sintering
MCHS	microchannel heat sink
PEI	polyetherimide
TO	topology optimization

a microchannel heat sink with integrated microjets. Their design showed 6 × increase in thermal conductance to pressure drop ratio compared to a baseline. Collins et al. [3] proposed a permeable membrane microchannel heat sink design that incorporated porous walls with the channel between capped at alternating the inlet and the outlet, forcing the coolant through the pores of the membrane walls. This novel design was 3D printed using DMLS in AlSi10Mg and showed a 17% reduction in thermal resistance and 28% reduction in pressure drop relative to a conventional straight channel design at a constant pumping power. Later, Ozguc et al. [4] performed a multi-objective parameter optimization of the permeable membrane microchannel heat sink design, which showed up to 68% lower thermal resistance at a set pressure drop compared to the straight channel heat sink. Kirsch and Thole [5] proposed wavy microchannels with interconnects and optimized the shape of the fins to improve the hydraulic and thermal performance of the heat sink. They fabricated a series of baseline and optimized designs using laser powder bed fusion in Inconel 718. The designs achieved a 6% reduction in friction factor when the pressure drop was minimized and a 9% increase in heat transfer when heat transfer was maximized. Numerous additional examples of AM-inspired, intuition-based designs can be found in the literature [6,7,8,9].

These intuition-based heat sink designs have shown performance enhancement, but as an alternative approach, various computational algorithms can numerically generate heat sink geometries to achieve higher performance. These algorithms excel when addressing complex design problems that are too difficult to solve using intuition alone, such as finding the best heat sink designs out of the endless possibilities enabled by additive manufacturing. Topology optimization (TO) is one such algorithm where material distribution within a design space is optimized to minimize or maximize a user-defined cost-function. Heat sink geometries have been generated using TO and shown to outperform conventional designs for various applications under different boundary conditions and governing flow physics. Li et al. [10] performed topology optimization for liquid-cooled heat sinks where the pressure drop was minimized and the heat exchange was maximized through a multi-objective optimization formulation. They investigated non-uniform heating conditions where the topology optimized design achieved an 11.7% lower maximum surface temperature compared to a straight fin/channel design. Dong and Liu [11] used multi-objective TO with three different objectives to generate air-cooled heat sink designs. Their design problem consisted of multiple heat sources and multiple coolant inlets, which would otherwise be challenging to solve using an intuition-based design. Alexandersen et al. [12] used 3D topology optimization to design natural-convection-cooled heat sinks. By using a parallel computing framework for solving the governing non-linear multi-physics system of equations, they were able to optimize up to 30 million design variables. Dilgen et al. [13] performed 3D TO of heat sinks with turbulent flow. Gilmore et al. [14] used 3D topology optimization to design the microchannels in the bottom layer of a two-layer manifold microchannel heat sink. The optimizer created structures that reduced the overall pressure drop by suppressing stagnation regions and limiting nozzle constrictions. Similarly, Zhou et al. [15] performed 3D, multi-objective TO of the bottom-layer microchannels in a manifold microchannel heat sink. The minimized cost function was defined as the weighted summation of the flow resistance and the average base plate temperature. Their topology optimized design outperformed a size-optimized rectangular channel/fin design along the Pareto optimality curve of the two weighted objectives. Sun et al. [16] conducted 3D topology optimization of liquid-cooled heat sinks using 6 million tetrahedral elements. Topology optimized design consisted of intricate features that routed the hot flow to the top and the cold flow to the bottom layer of the heat sink. This design showed a 10-40% lower temperature compared to an optimized parallel plate fin heat sink under the same pumping power.

Despite their significant performance advantages, topology optimized designs are often too complex in geometry to fabricate using conventional manufacturing approaches. Therefore, additive manufacturing and topology optimization have been proposed to be used in conjunction where high-performance parts can be designed with TO and the resulting complex geometries can be fabricated using AM. Dede et al. [17] generated topology optimized air-cooled heat sinks and fabricated them using additive manufacturing out of AlSi12. Relative to a series of conventional designs, the optimized heat sink design showed a higher coefficient of performance (defined as the inverse of the product of thermal resistance and pumping power). Han et al. [18] topology optimized

liquid-cooled heat sinks for a design space with multiple inlets and outlets which showed up to 57% reduced temperature difference within the heat sink compared to the temperature difference of their benchmark, a spider-web-like heat sink design; one of the designs was 3D printed in aluminum for experimental demonstration. Joshi et al. [19] performed an experimental comparison of a topology optimized multi-pass branching microchannel heat sink fabricated using additive manufacturing and conventional machining. The AM part showed a 46% increase in cooling performance at the cost of a 91% increase in pressure drop, which was attributed to the high surface roughness of AM microchannels. Lazarov et al. [20] used topology optimization to generate passively cooled heat sink designs for cooling LED lamps. A resulting design was 3D printed and experimental comparisons showed a 21% lower temperature rise relative to the benchmark lattice heat sink geometries.

In commonly used topology optimization approaches, the design variables represent the spatial porosity distribution of a fictitious porous media; intermediate porosity values are penalized during optimization such that the final designs consist of strictly solid and fluid regions. Recently, Ozguc et al. [21] proposed a homogenization approach to topology optimization where the design variables represent the dimensions of physical microstructures that make up the design space. The homogenization approach thereby does not require any penalization as the resulting designs consist of microstructures with spatially varying dimensions over the full spectrum of design variable values. Implementation of these microstructures using porous-media-based flow and heat transfer equations allows their features to be smaller than the numerical discretization, and hence, the homogenization approach can generate heat sink designs with sub-grid-resolution features. This is especially advantageous in the multi-scale design of large liquid-cooled heat sinks where the optimum fin and channel sizes are on the order of 10s of microns within practical pressure drop ranges of 1-10 kPa. Additionally, the microstructure in the homogenization approach can be chosen to align with the capabilities of the AM process that will be used for fabrication, leading to heat sink designs that can be 3D printed with minimal post-processing. Lastly, the penalization methods commonly used in TO approaches rely on hyperparameters that significantly affect the end design and must be tuned by experienced users. The homogenization approach does not use penalization and therefore requires much less input from the user to generate a feasible design. These advantages make the homogenization approach to topology optimization well-suited for the design of high-performance, additively manufactured microchannel heat sinks.

The homogenization approach was proposed by Ozguc et al. [21]. An initial demonstration showed that the topology optimized designs generated using the homogenization approach were able to theoretically achieve lower pressure drop and thermal resistance compared to the optimized straight channel heat sink at a given flow rate. The homogenization approach shows great promise, however, there is a need to better understand and experimentally demonstrate the process of translating the topology optimized design from theory into a functioning 3D printed heat sink. The work presented here addressing this need will be introduced as follows: (1) the homogenization approach is first used to generate a series of topology optimized liquid-cooled microchannel heat sink designs using different grid resolutions, (2) heat sink samples are fabricated to determine the grid feature resolutions that are possible within the AM capabilities, (3) a non-intrusive post-processing approach is developed to create AM-ready designs based on the fabrication constraints, and lastly, (4) a series of optimized heat sinks were fabricated and their performance experimentally demonstrated to lie along the predicted Pareto optimality curve.

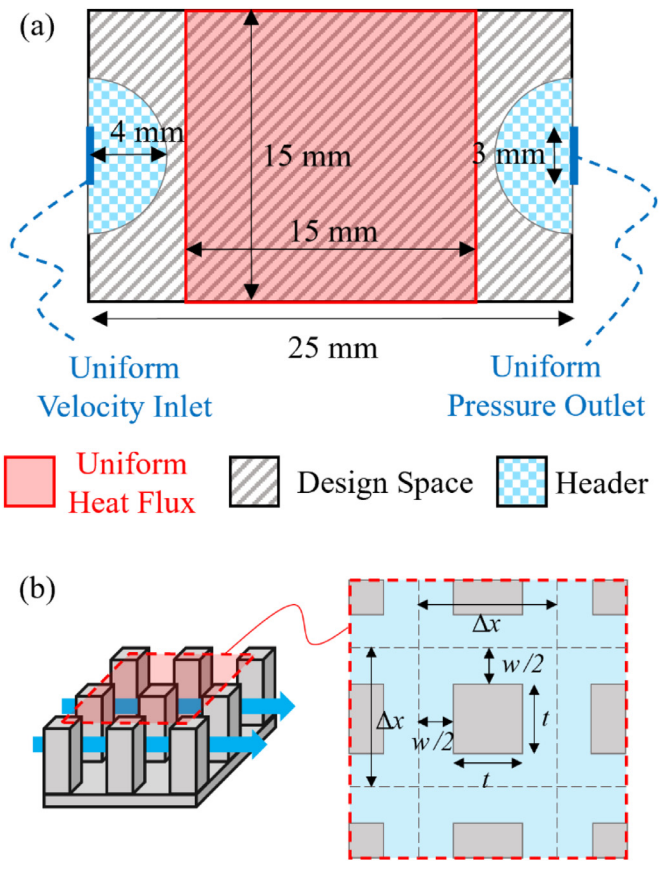

Fig. 1. (a) Schematic drawing of the 2D design space and boundary conditions used for topology optimization of the microchannel heat sinks, and (b) the schematic drawings of the user-defined microstructures used in the homogenization approach.

2. Methodology

2.1. Topology optimization

The design problem is defined as the minimization of a user-defined cost function by optimizing the material distribution within a design space for a set of boundary conditions. The 2D design space and the boundary conditions used for topology optimization are shown in Fig. 1a, which represents a top-down view of where the microchannel heat sink (MCHS) would be placed. Flow enters with a uniform velocity through the inlet on the left edge and leaves from the uniform pressure outlet on the right edge. A uniform heat flux boundary condition is applied over a 15×15 mm^2 area centered within the design space. Semi-circular headers with a 4-mm radius are imposed at the inlet and the outlet. The optimizer is not allowed to modify the material distribution inside the header regions, which are left completely open (no solid material) to provide locations for pressure measurement near the inlet and the outlet during experimental testing. A solid base thickness (H_b) of 3 mm and a fin/channel height (H) of 1 mm are used for the current design cases, resulting in an overall MCHS thickness of 4 mm. The thickness of the solid base is chosen so that thermocouples can be easily embedded at the centers of the MCHS designs during experimental testing.

A homogenization approach to topology optimization is used with user-defined microstructures that represent the partial densities in topology optimization. Similar to Ozguc et al. [21], square pin fins of varying thickness and gap size are used as the microstructure. Schematic drawings of this chosen microstructure are shown in Fig. 1b and the design variable is formulated as follows.

Table 1
Properties of water evaluated at 30 °C [23].

ρ (kg/m^3)	μ (Pa·s)	c_p (kJ/kg)	k (W/(m·K))
995.8	$803.4 \cdot 10^{-6}$	4.178	0.6172

$$\varepsilon_i = \frac{\Delta x - t_i}{\Delta x} = \frac{w_i}{\Delta x} \tag{1}$$

With this formulation, the MCHS design space is discretized into grid cells of size Δx, where each grid consists of a single square pin fin of thickness t. The thickness of each fin is then modified iteratively by the optimizer through the design variables ε_i of each cell to minimize a user-defined cost function.

The total heat input (Q) does not affect the resulting TO designs because the governing energy conservation equation is linear; temperature-rise scales linearly with heat input and thermal resistance stays constant. Therefore, optimization and testing of the designs are performed at a single heat input and are not repeated for different values. Total heat input of 60 W is chosen to ensure that the heater temperature does not rise above the melting point of the polyetherimide (PEI) insulating material used in the experimental facility. The heat sink material is AlSi10Mg with an assumed thermal conductivity of 160 W/m-K in the middle of the range provided by the supplier (130-190 W/m-K [22]). The coolant is water (with the properties shown in Table 1) that enters the design space at 30 °C at a flow rate ($\dot{V}$) of 200 mL/min.

Both pressure drop (ΔP) and thermal resistance (R) are important metrics for evaluating the performance of a heat sink design. Pressure drop is defined as the difference in the static pressure of the coolant between the inlet and the outlet. The thermal resistance is calculated from the maximum base temperature (T_{max}) and the coolant inlet temperature ($T_{c,in}$) as

$$R = \frac{T_{max} - T_{c,in}}{Q} \tag{2}$$

This thermal resistance formulation uses the maximum heat sink base temperature, the location of which can change during optimization. This leads to an ill-posed optimization problem and therefore a weighted thermal resistance formulation shown is instead used during topology optimization, as calculated from the base temperature distribution (T_b) where higher temperatures have a higher impact on the resistance.

$$R_w = \frac{\left[\frac{1}{A_b}\iint (T_b - T_{c,in})^4 dA\right]^{1/4}}{Q} \tag{3}$$

The weighting operation was performed by using an exponent of 10 in our previous work [21] for which there was a small hot spot within the design space, which fixed the location of the peak temperature. A smaller value of 4 is more suitable for the large uniform heat flux boundary condition used in this study because the location of the peak temperature in the domain is expected to change throughout the optimization, which can lead to an ill-posed problem if the exponent is too high. A multi-objective optimization approach is used to account for the competing pressure drop and thermal resistance metrics. The cost function shown is taken as the weighted summation of these two objectives.

$$f_{cost} = m \cdot \frac{\Delta P - \bar{P}}{\bar{P}} + (1 - m) \cdot \frac{R_w - \bar{R}}{\bar{R}} \tag{4}$$

where the weighting coefficient (m) is a user-defined value between 0 and 1. The pressure drop and thermal resistance are normalized by the normalizing constants $\bar{P}$ and $\bar{R}$ chosen as 2.5 kPa and 0.1 K/W respectively. Such normalization is common in multi-objective optimization problems and the values of these constants determine the correspondence between the weighting factor and the performance of an individual design; however, they do not affect the Pareto optimality curves created by a collection of designs generated by varying the weighting factor from 0 to 1.

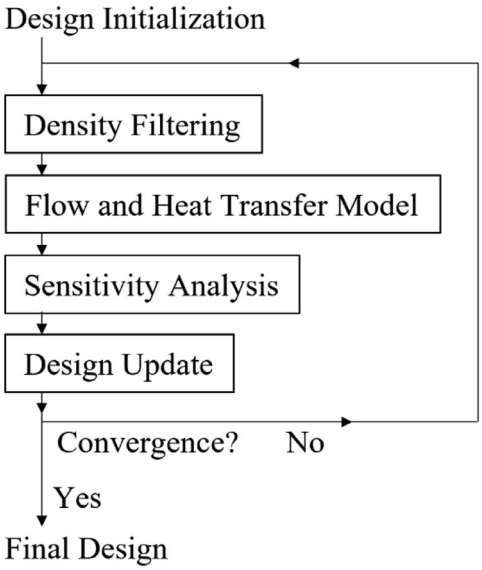

Fig. 2. Schematic diagram of the TO process flow.

Topology optimization is an iterative process wherein the design variables are updated at each iteration to reduce the value of the cost function. Fig. 2 shows a schematic diagram of the TO process flow. A brief description of each step is provided with relevant references as follows.

1. Design Initialization: A user-defined design space with specified boundary conditions is discretized into square grid cells. Each grid cell holds a square pin fin represented by the design variable ε_i defined in Eq. (1). In this work, each design variable is initialized to a value of 0.90. Ozguc et al. [21] showed that different initializations result in different designs, as is expected in topology optimization problems, but more importantly the performance differences between such designs are negligible.
2. Density Filter: The designs are filtered using the density filtering scheme described by Sigmund [24] to avoid checkerboard patterns, which is formulated as follows.

$$\varepsilon_{f,j} = \frac{\sum w_f(x_i)\varepsilon_i}{\sum w_f(x_i)} \tag{5}$$

$$w_f(x_i) = R_f - \left\| x_i - x_j \right\| \tag{6}$$

where subscripts i and j represent the design variable index, ε_f is the filtered design variable, x is the position of a design variable, $w_f(x_i)$ is the weight of a design variable on the filtering operation, and R_f is the filter radius. A filter radius of $1.5 \times \Delta x$ is used which includes only the neighboring cells. This is found to be adequate to avoid checkerboard patterns without constraining the optimizer with a larger filter radius.

3. Flow and Heat Transfer Model: The TO algorithm can only create designs that vary over the footprint and are uniform along the height. However, the governing "2.5D" physical models used in this work account for certain 3D effects, namely, heat spreading in the solid base layer and the changes in momentum, viscous shear, and energy capacity due to the presence of assumed velocity and temperature profiles along the height direction. A detailed description of the governing mass, momentum, and

energy equations with corrections for these 3D effects achieved by a height-averaging operation on the governing equations is given in Refs. [21] and [25]. Inherently, these are porous media models where source terms with effective porous media properties such as permeability, surface area density, effective conductivity, and internal convection coefficient are used to model the microstructure shown in Fig. 1b. The model formulation accounts for thermal non-equilibrium within each grid cell to solve for velocity, pressure, and temperature fields throughout the design domain.

4. Sensitivity Analysis: Gradients of the cost function with respect to the design variables are calculated using the adjoint state method [26].
5. Design Update: The gradient information is used with the Sequential Linear Programming (SLP) algorithm [27] to modify the MCHS design at each iteration to minimize the cost function defined in Eq. (4).
6. Convergence: A convergence criteria can be defined to automatically end the optimization. In the current work, a fixed number of 200 iterations is used for all the designs generated. It was observed that this was sufficient for the cost function value and the design variables to stop changing long before the maximum number of iterations is reached.

2.2. Experimental methods

Direct metal laser sintering was used for the fabrication of the pin fin samples and the heat sinks. To characterize the pressure drop and thermal resistance of the TO designs, an experimental facility was constructed as shown in Fig. 3a. Deionized water in the reservoir flows through air-to-liquid heat exchangers to remove the heat accumulated along the flow loop. A positive displacement gear pump is used to circulate the fluid (Micropump GC-M23.JDS.E pump-head with Baldor 1/3 HP, 3PH inverter duty motor). A bypass line creates a direct flow path between the pump and the reservoir to assist in controlling the flow rate through the rest of the flow loop using a needle valve. The flow through the primary path passes through particulate and carbon filters to remove any possible contaminants. The flow rate to the test section is measured using a Coriolis mass flow meter (Micro Motion CMFS010M). Liquid-to-liquid heat exchangers preheat the coolant to the desired inlet temperature of 30 °C. The secondary flow through the heat exchangers is a water-ethylene glycol line connected to a constant temperature bath (Thermo Scientific AC200) with a built-in pump. After passing through the test section, the outlet stream returns to the reservoir.

The test section is depicted in greater detail in Fig. 3b. It consists of a 12.5 × 12.5 mm^2 ceramic heater positioned inside a PEI spacer. The heater is attached on its bottom surface to the spacer using an RTV silicone. A 5 × 15 × 15 mm^3 copper block is placed on top of the ceramic heater with thermal grease in between. Another layer of thermal grease connects the copper block with a heat sink centered on top. The heater-heat sink assembly is compressed using a polycarbonate block on the top and a PEI base plate at the bottom using four spring-loaded bolts tightened around the corners. The polycarbonate block contains flow features to route the coolant through the heat sink from the inlet and outlet ports. A silicone rubber sheet is placed in between the polycarbonate block and the heat sink to maintain a hydraulic seal of this flow path.

A differential pressure transmitter (Omega, PX2300-2DI, 0-2 PSI, 24 V, 4-20 mA) measures the pressure drop between the two pressure taps which connect to the headers of the heat sink. The flow temperature is measured at the test section inlet and outlet using T-type thermocouples. The temperature of the ceramic heater (T_{heater}) is measured using an embedded K-type thermocouple. The

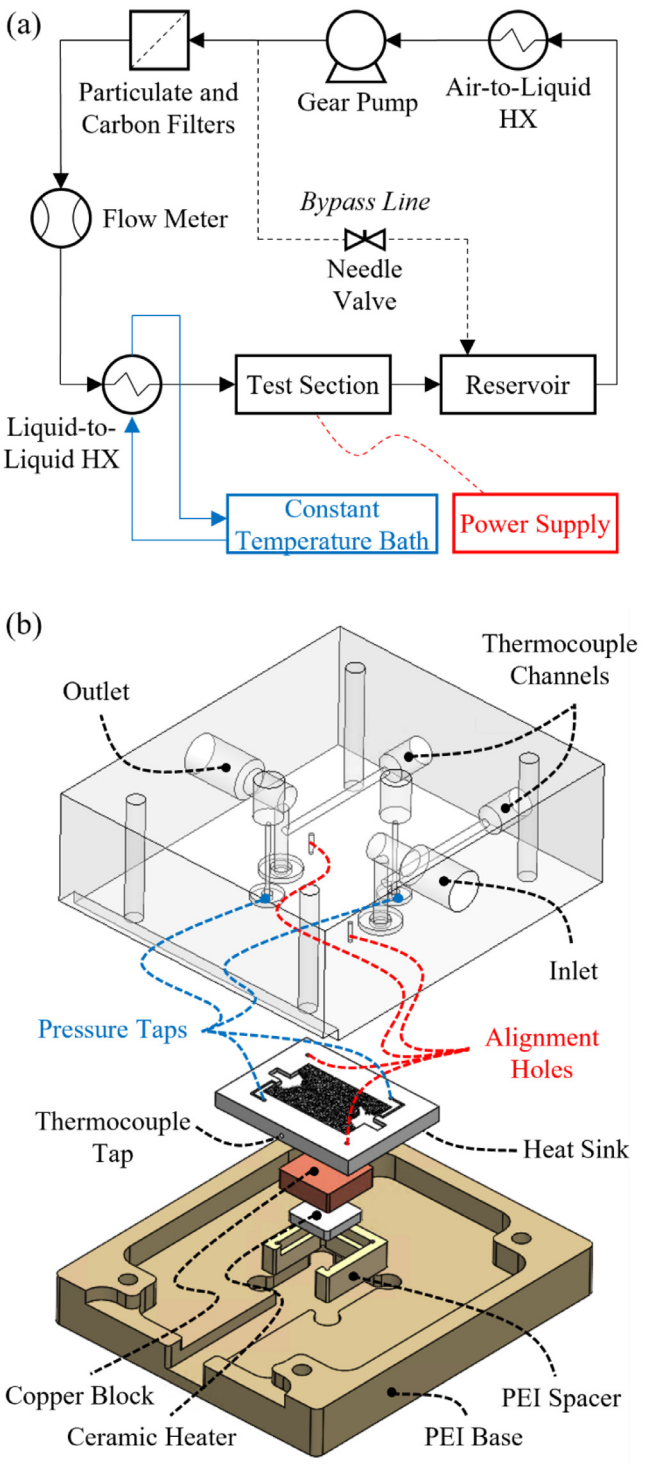

Fig. 3. (a) Schematic diagram of the flow loop facility and (b) exploded drawing of the test section.

heater is powered by a DC power supply (Sorensen XG 100-8.5). The electrical current provided by the power supply is calculated by measuring the voltage drop across a shunt resistor (HA-5-50, Empro, 0.01 Ω) connected in series with the heater. The total power input is then calculated from the current and the voltage drop across the heater. A T-type thermocouple probe is inserted into a hole embedded into the center of the base of the heat sink (T_{exp}). Another T-type thermocouple is used to continuously monitor the ambient temperature during testing. An ice-point reference

(Omega TRCIII) is used as the reference junction of the T-type thermocouples which are calibrated before testing using a dry block calibrator (Jupiter 4852, Isotech). The temperature of the ice-point reference is measured using an RTD temperature sensor. Measurements are taken at 1 Hz and recorded using a data acquisition system (NI cDAQ-9178 with modules NI-9217, NI-9208, NI-9205, and NI-9214).

All the heat sinks are tested at a flow rate of 200 mL/min entering at 30 °C, and with a total heat input of approximately 60 W after subtracting the estimated heat losses from the insulation. First, a heat sink is installed into the test section shown in Fig. 3b. The pump, the constant temperature bath, and the power supply are turned on and set to the desired operating conditions. Steady state conditions are achieved when the temperatures at the flow inlet/outlet, heat sink base, and heater have standard deviations of less than 0.05 K for 1 min. Pressure drop across the heat sink, inlet/outlet flow temperatures, heat sink base temperature, heater temperature, ambient temperature, flow rate, and heat input are recorded when a steady state is reached. An average of 60 data points is recorded for all measurement signals.

The parasitic heat losses from the heater to the surrounding ambient are calibrated by measuring the heater temperature when heat is applied without the circulating coolant. For this calibration, the heat input is gradually increased, and the resulting steady state temperature of the heater is measured. The heat input is increased at 1 W intervals until the heater reached 145°C. Linear regression is used to correlate the heat loss with respect to the temperature difference between the heater and the ambient. The following resulting correlation has an R^2 value of 0.999.

$$Q_{loss} = 0.0553\frac{W}{K} \cdot (T_{heater} - T_{\infty}) \tag{7}$$

where Q_{loss} is the parasitic heat losses, T_{heater} is the heater temperature, and T_{∞} is the ambient temperature. The maximum heat loss observed during the testing of the heat sinks was 6.6% of the input power. Net heat into the coolant through a heat sink during testing is calculated by subtracting the heat loss from the total heat input.

2.3. Data reduction

The pressure drop of the heat sink under test is directly measured and no calculations are performed on the measurement. The thermal resistance defined based on the maximum heat sink base temperature (Eq. (2)) cannot be evaluated from the experiments because the temperature profile is not measured. Instead, a single temperature measurement is taken from the center of the base of a heat sink (T_{exp}). A testing thermal resistance (R_{exp}) is instead calculated from the temperature and heater power measurements as follows.

$$R_{exp} = \frac{T_{exp} - T_{c,in}}{Q - Q_{loss}} \tag{8}$$

This testing thermal resistance is used whenever the model predictions are compared to experimental results, as T_{exp} can be trivially extracted from the model. The error bars included in the experimental results are estimated with the propagation of uncertainty using the random error in the measurements and the systematic error of the sensors provided by the manufacturers. Details on the uncertainty analysis can be found in the supplemental material section S1.

3. Results

The multi-objective cost function defined in Eq. (4) is the weighted summation of pressure drop and thermal resistance,

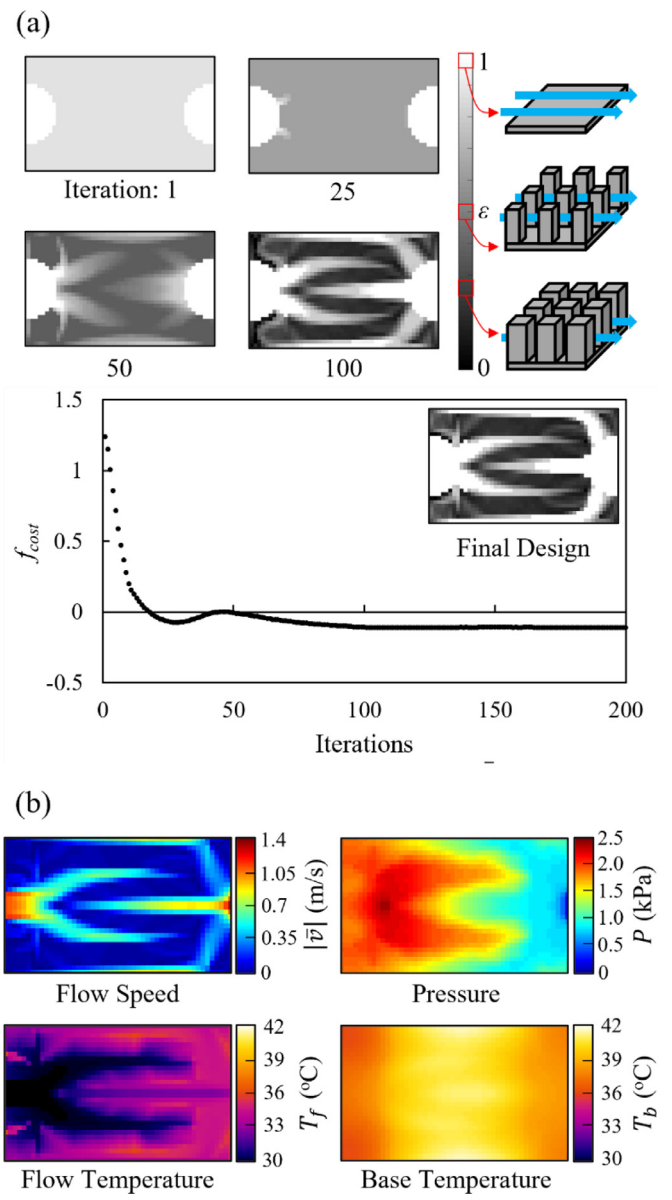

Fig. 4. (a) Material distribution maps of the microchannel heat sink designs and plot of the cost function with increasing topology optimization iterations; design generated using a weighting coefficient of $m = 0.835$. (b) The resulting flow speed, pressure, flow temperature, and base temperature contour maps for the final design after 200 iterations.

where the weighting coefficient ($0 < m < 1$) represents the importance given to one objective over the other. Fig. 4a shows the evolution of a MCHS design and the cost function value with the number of iterations during optimization generated using a weighting coefficient of $m = 0.835$ and a grid size of 0.5 mm. The cost function value appears to converge to a nearly constant value after approximately 100 iterations. The design at iteration 100 looks very similar to the final design at iteration 200, however, some slight differences provide a minor further reduction in the cost function. Note that the cost function value can attain a negative value when the thermal resistance or pressure drop is sufficiently below their respective normalizing constants as defined in Eq. (4). The final design consists of continuous open channels (white regions) that start from the inlet and the outlet and branch into multiple smaller channels. Inlet-side and outlet-side branches are separated by wide boundaries of tightly packed pin fins (dark grey regions). Fig. 4b shows the resulting flow speed, pressure, flow temperature,

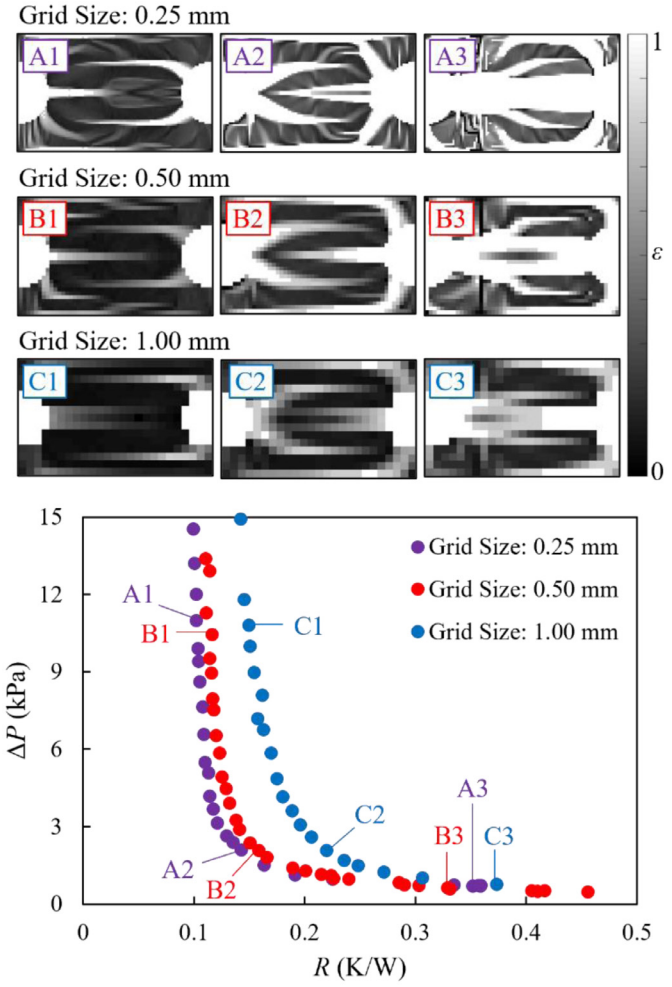

Fig. 5. Pareto optimality curves generated using three different grid cell sizes and material distribution maps of three designs from each curve.

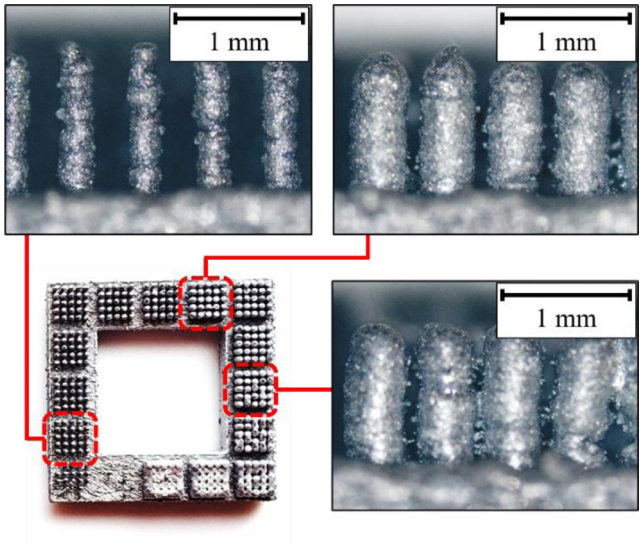

Fig. 6. Top-down photograph of a sample print with a 0.5 mm grid cell size and pin fin arrays of varying thicknesses. Side-view optical microscopy images of 0.245 mm, 0.402 mm, and 0.412 mm thick pin fin arrays are shown (in clockwise order).

and base temperature maps for the final design. The flow speed is high near the inlet and the outlet but decreases gradually along the branches as the coolant is pushed through the pin fin array. There is a steep pressure gradient across the tightly packed pin fins separating the inlet and outlet branches, which causes a slow but uniform flow speed. The flow temperature map indicates that the majority of the heat is removed from the heat sink as the coolant is pushed through the tightly packed pin fins. The branching open channels resemble a single layer manifold structure with the purpose of distributing the coolant along the heat sink with minimal flow resistance; meanwhile, the tightly packed pin fins are designed to remove the heat uniformly with high convective heat transfer performance.

Square grid cells are used for discretization of the governing partial differential equations, but each grid cell also contains a single square pin fin as shown in Fig. 1b. Therefore, the grid cell size affects the size of the pin fins; smaller grid cells will result in smaller pin fins. Topology optimized designs are generated using three different grid cell sizes of 0.25 mm, 0.5 mm, and 1 mm to investigate the effect on the resulting designs and performance. Pareto optimality curves are created for each grid resolution by generating a series of designs with weighting coefficients varying from 0 to 1. Fig. 5 shows the resulting Pareto optimality curves and the material distribution maps for three designs from each curve. Each point shown on a Pareto optimality curve is a topology optimized design generated using a different weighting coefficient. Regardless of the grid size used, larger weighting coefficients lead to higher pressure drop designs that generate more pin fins with tighter spacing (darker material distribution maps) to achieve lower thermal resistance. Conversely, smaller weighting coefficients lead to lower pressure drop designs having more open channels. At very low pressures, the designs have continuous flow paths that connect directly from the inlet to the outlet such that the coolant can bypass all the pin fins. As a result, these low-pressure-drop designs have greatly deteriorated thermal performance (high thermal resistance). The performance of the resulting designs is affected by the grid resolution. The 1.00 mm grid cell size has the worst performance as it has the highest thermal resistance at a given pressure drop or the highest pressure drop at a given thermal resistance. The performance improves with reducing grid cell size down to the smallest 0.25 mm size that has the best performance; however, the performance improvement has notably diminishing returns, with only a marginal improvement seen when reducing from 0.50 mm to 0.25 mm grid cell size.

Even though smaller grid cell sizes improve performance, the fabrication capabilities of metal AM processes also need to be considered. A series of samples with pin fins are 3D printed using grid cell sizes of 0.25 mm, 0.35 mm, 0.4 mm, and 0.5 mm. Each sample has arrays of pin fins of varying thicknesses so that the design variable range ($0 \leq \varepsilon_i \leq 1$) is captured at each grid resolution. For all the grid resolutions, pin fins smaller than ~0.245 mm did not survive the fabrication process. This resulted in smaller grid cell sizes having a narrower printable design variable range; for example, the 0.5 mm grid cell size can achieve $0 \leq \varepsilon_i \leq 0.51$ and 0.35 mm grid cell size can only achieve $0 \leq \varepsilon_i \leq 0.3$. In general, samples with a 0.5 mm grid cell size provided the most consistent sample-to-sample prints. This largest grid cell size also gives the largest 3D printable design variable range, albeit at the cost of reduced heat sink performance. Nevertheless, in the interest of facilitating a comparison between the predicted performance of the TO designs and measurements, the 0.5 mm grid cell size is chosen for the experimental investigation.

Fig. 6 shows a top-down photograph of the sample print with 0.5 mm grid cell size and side-view optical microscopy images of three different arrays of pin fins, each with a different fin thickness. The smallest pin fin thickness array shown in Fig. 6 is at the aforementioned threshold of the thickness (0.245 mm) that is

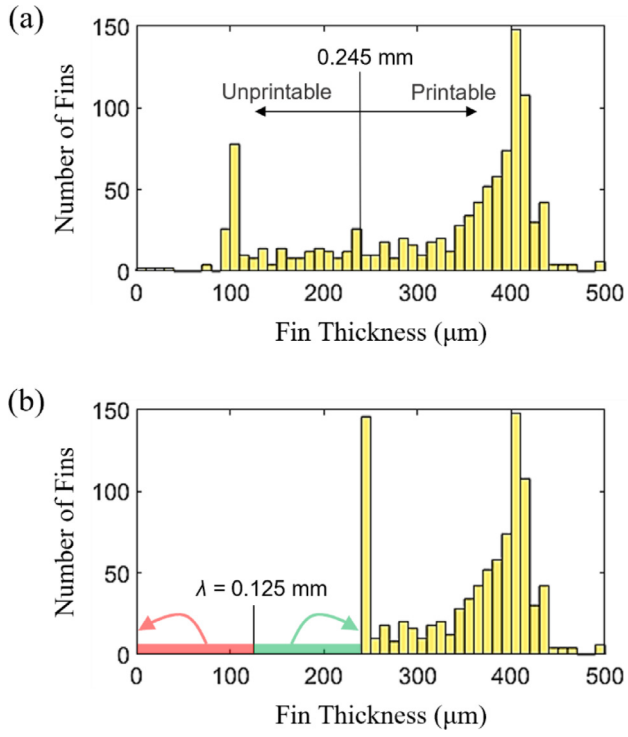

Fig. 7. Histogram of fin thicknesses within the topology optimized design shown in Fig. 4: (a) before and (b) after post-processing.

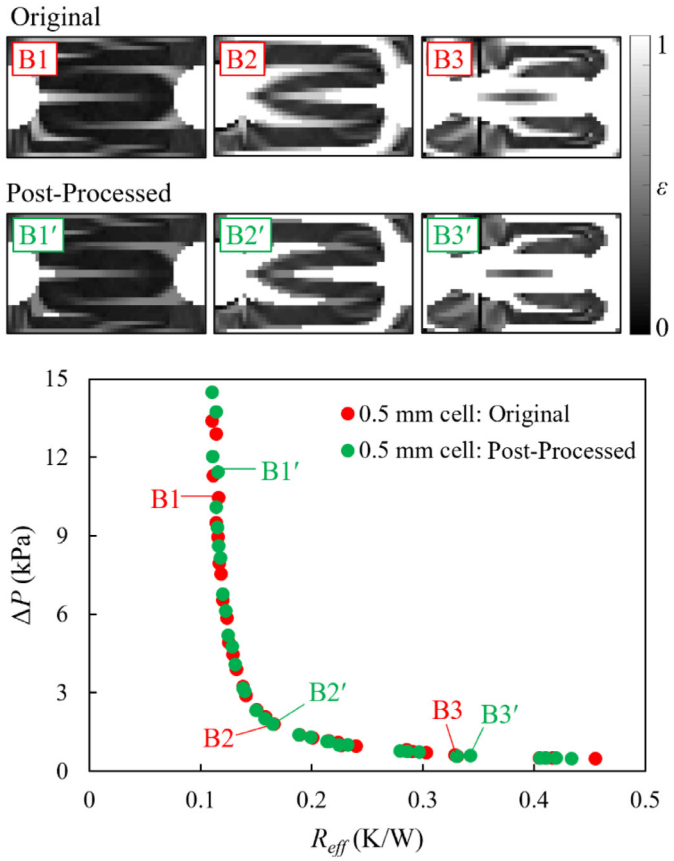

Fig. 8. Pareto optimality curves for 0.5 mm grid cell size before and after post-processing with material distribution maps of three designs.

printed consistently sample-to-sample. Although the pin fins are designed to be square in their cross sections with sharp corners, the 3D printed fins are circular. This is attributed to the circular laser spot size that is on the order of the pin fin thicknesses. Additionally, a high surface roughness (Ra ≈ 17.4 μm [4]) can be seen in the microscopy images which creates connections between thick pin fins with small channels. This is expected to create a more tortuous flow path that will improve convective heat transfer performance at the cost of increased pressure drop compared to the model predictions that assume smooth, separate pin fins. Despite differences compared to the fin geometry that is modeled during optimization, the homogenization approach is not specific to a single geometry and the model of the microstructure can be adjusted to match the geometry and properties associated with any available fabrication process.

The minimum printable fin thickness associated with the process used in this work is 0.245 mm. Therefore, the resulting topology optimized designs are post-processed to remove the pin fins thinner than 0.245 mm before fabrication, and the model is re-run on the post-processed designs to ensure minimal effect on the performance. Fig. 7a shows a histogram of all fin thicknesses within the topology optimized heat sink design shown in Fig. 4, excluding the open channels ($t = 0$). A simple post-processing step has been developed to make the designs fabricable and conserve optimal performance. A thresholding thickness (λ) is defined where any pin fins thinner than the threshold ($t < \lambda$) are removed. Any pin fins thicker than the threshold but thinner than the fabrication thickness limit ($\lambda < t < 0.245$ mm) are set equal to the 0.245 mm limit. Several values of thresholding thickness are tried and $\lambda = 0.125$ mm is found to result in post-processed designs with negligible performance deviation from the optimal. Fig. 7b shows the fin thickness distribution of the design from Fig. 4 after the post-processing step is performed.

All of the topology optimized designs from along the Pareto optimality curve for a 0.5 mm grid cell size (Fig. 5) are post-processed using a threshold thickness of $\lambda = 0.125$ mm. Fig. 8 shows the original Pareto optimality curve and the performance curve of the designs after post-processing, with material distribution maps of several designs also shown before and after post-processing. Although individual points on the Pareto curve are slightly shifted along the curve, the performance of the Pareto optimality curve is preserved.

Ten post-processed, topology-optimized designs along the Pareto optimality curve are fabricated using DMLS of AlSi10Mg. Fig. 9 shows the material distribution map for one representative design ($\Delta P = 1.107$ kPa, $R = 0.224$ K/W) and two photographs of the corresponding 3D printed heat sink. A complete set of images of the rest of the fabricated designs is available in the supplemental material section S2. All the printed parts look the same as the designs generated by the TO algorithm with minor artifacts.

The fabricated heat sinks are tested experimentally to measure their pressure drop and thermal resistance. Fig. 10 shows the resulting experimental data plotted over top of the Pareto optimality curve from the numerical predictions. Only the designs that were printed and tested are shown on the numerical Pareto optimality curve and each experimental data point corresponds to one of the designs. The axes shown in Fig. 10 are the experimentally measured pressure drop (ΔP_{exp}) and the measured thermal resistance (R_{exp}), which are different from the pressure drop and the thermal resistance used in the cost function in Eq. (4). The measured pressure drop is the pressure difference between the exact location of the experimental pressure taps, which are connected to the inlet and outlet headers near the inlet and the outlet. Due to the placement of the pressure taps, it is possible for the measured pressure difference to be negative because of a local rise in pressure near the pressure tap downstream. The testing thermal resistance is cal-

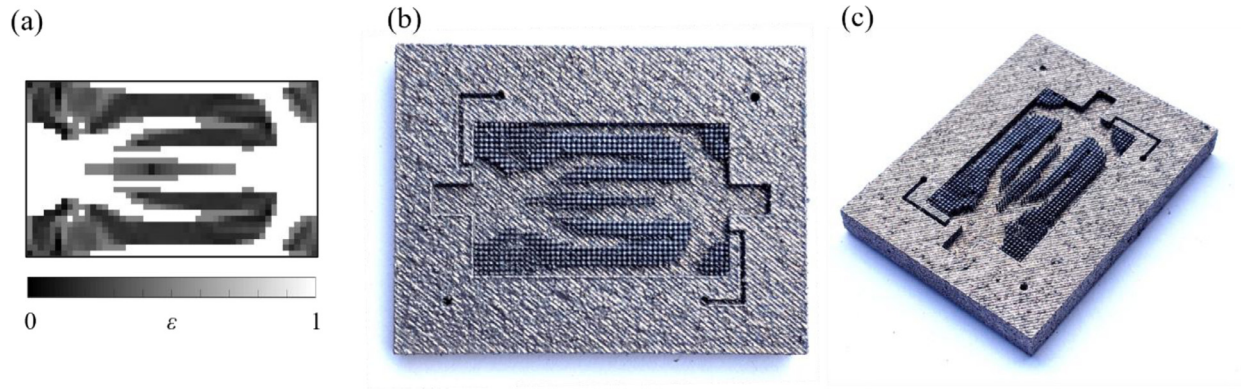

Fig. 9. (a) Post-processed material distribution map of a TO design from the Pareto optimality curve for 0.5 mm grid cell size. (b) Top-down and (c) isometric photographs of the topology optimized, 3D printed microchannel heat sink.

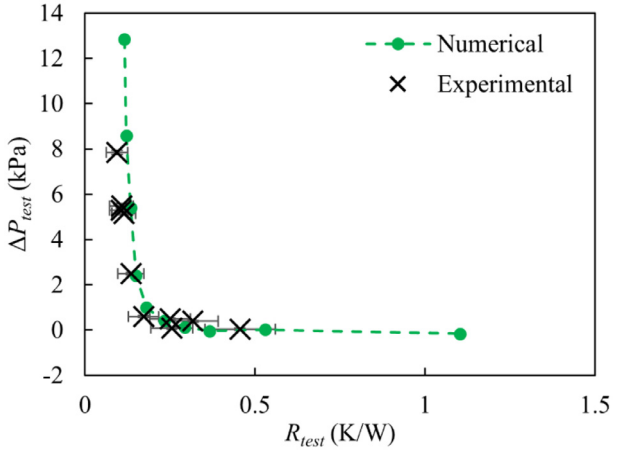

Fig. 10. Performance comparison of the numerical Pareto optimality curve generated by the topology algorithm and the experimental results obtained from the testing of the 3D printed microchannel heat sink designs.

culated from the thermocouple measurement taken at the center of the heat sink base was defined and discussed in Eq. (8).

The first prominent observation from Fig. 10 is that the Pareto optimality curves formed by the numerical and experimental data lay on top of each other. Furthermore, there is a direct correspondence in the order of the experimental and numerical data with respect to thermal resistance, namely, the design predicted to have the lowest thermal resistance corresponds with the measurements, and so forth. Despite the overlap in the optimality curves, there are notable differences between the exact values of numerical predictions and the experimental results (i.e., the measured performance is shifted along the curve compared to the predictions). This is generally attributed to the geometric differences between the modeled and printed pin fins. First, although the macroscale topology and arrangement of the printed fins look visually similar to the optimized designs, the dimensions of the pin fins do not match exactly. Furthermore, there are shape differences between the modeled square pin fins with smooth walls and the 3D printed pin fins which are more circular with high surface roughness. As the rounded edges of the printed fins would tend to lower the pressure drop whereas the high surface roughness would increase the pressure drop, there is not a consistent direction observed in the shift along the Pareto curve. Further discussion of point-to-point mismatch between the Pareto curves is included in the supplemental material Section S3. Nevertheless, the TO algorithm and model successfully guide the designs to create Pareto-optimal 3D printed parts.

4. Conclusions

The design freedom brought by additive manufacturing can be leveraged by topology optimization algorithms to create high-performance heat sinks with intricate features. This work used a homogenization approach to topology optimization to design microchannel heat sinks consisting of spatially varying 3D printing-friendly pin fin microstructures. A multi-objective cost function with the objectives of minimum pressure drop and minimum thermal resistance was used to generate a series of Pareto-optimal designs. The effect of grid cell size used for discretization of the design space was investigated, in combination with the printing capabilities of a commercial DMLS process, to determine a practical grid resolution for the 3D printed microchannel heat sinks. A set of ten topology optimized heat sinks along the predicted Pareto curve were fabricated, experimentally tested, and compared to the model predictions. This work demonstrates a process for considering additive manufacturing print feature size limits in the optimization process; the homogenization approach enables a direct translation of topology optimization results into 3D printable designs that lie on the Pareto front. The experimental results showed a good match between the numerical Pareto front and the 3D printed microchannel heat sinks with minor differences due to the geometric differences between the 3D printed and modeled fins, and the unaccounted hydraulic and thermal developing effects. Additional work to tune the models for flow and heat transfer within additively manufactured microstructures will allow a direct TO-to-reality design process for microchannel heat sinks.

Declaration of Competing Interest

The authors declare that they have no known competing financial interests or personal relationships that could have appeared to influence the work reported in this paper.

CRediT authorship contribution statement

Serdar Ozguc: Conceptualization, Methodology, Software, Investigation, Writing – original draft, Visualization. **Trevor F.G. Teague:** Investigation, Writing – review & editing. **Liang Pan:** Conceptualization, Writing – review & editing, Supervision. **Justin A. Weibel:** Conceptualization, Writing – review & editing, Supervision.

Data Availability

Data will be made available on request.

Acknowledgements

Financial support for this work provided by members of the Cooling Technologies Research Center, a graduated National Science Foundation Industry/University Cooperative Research Center at Purdue University, is gratefully acknowledged.

Supplementary materials

Supplementary material associated with this article can be found, in the online version, at doi:10.1016/j.ijheatmasstransfer.2023.124108.

References

[1] M. Fasano, L. Ventola, F. Calignano, D. Manfredi, E.P. Ambrosio, E. Chiavazzo, O. Asinari, Passive heat transfer enhancement by 3D printed Pitot tube based heat sink, International Communications in Heat and Mass Transfer 74 (2016) 36–39.
[2] R. Kempers, J. Colenbrander, W. Tan, R. Chen, A.J. Robinson, Experimental characterization of a hybrid impinging microjet microchannel heat sink fabricated using high-volume metal additive manufacturing, International Journal of Thermofluids 5-6 (2020) 100029.
[3] I.L. Collins, J.A. Weibel, L. Pan, S.V. Garimella, A permeable-membrane microchannel heat sink made by additive manufacturing, International Journal of Heat and Mass Transfer 131 (2019) 1174–1183.
[4] S. Ozguc, L. Pan, J.A. Weibel, Optimization of permeable membrane microchannel heat sinks for additive manufacturing, Applied Thermal Engineering 198 (2021) 117490.
[5] K.L. Kirsch, K.A. Thole, Numerical optimization, characterization, and experimental investigation of additively manufactured communicating microchannels, Journal of Turbomachinery 140 (11) (2018) 111003.
[6] M. Baldry, V. Timchenko, C. Menictas, Optimal design of a natural convection heat sink for small thermoelectric cooling modules, Applied Thermal Engineering 160 (2019) 114062.
[7] S. Otake, Y. Tateishi, H. Gohara, R. Kato, Y. Ikeda, V. Parque, M.K. Faiz, M. Yoshida, T. Miyashita, Heatsink design using spiral-fins considering additive manufacturing, in: 2019 International Conference on Electronics Packaging, 2019, pp. 46–51.
[8] Y. Tateishi, V. Parque, T. Miyashita, H. Gohara, R. Kato, Y. Ikeda, Design optimization of heat sink using additive manufacturing, in: 2017 IEEE CPMT Symposium Japan, 2017, pp. 91–94.
[9] P.-H. Tseng, K.-T Tsai, A.-L. Chen, C.-C. Wang, Performance of novel liquid–cooled porous heat sink via 3-D laser additive manufacturing, International Journal of Heat and Mass Transfer 137 (2019) 558–564.
[10] H. Li, X. Ding, F. Meng, D. Jing, M. Xiong, Optimal design and thermal modelling for liquid-cooled heat sink based on multi objective topology optimization: An experimental and numerical study, International Journal of Heat and Mass Transfer 144 (2019) 118638.
[11] X. Dong, X. Liu, Multi-objective optimal design of microchannel cooling heat sink using topology optimization method, Numerical Heat Transfer, Part A: Applications 77 (1) (2020) 90–104.
[12] J. Alexandersen, O. Sigmund, N. Aage, Large scale three-dimensional topology optimisation of heat sinks cooled by natural convection, International Journal of Heat and Mass Transfer 100 (2016) 876–891.
[13] S.B. Dilgen, C.B. Dilgen, D.R. Fuhrman, O. Sigmund, B.S. Lazarov, Density based topology optimization of turbulent flow heat transfer systems, Structural and Multidisciplinary Optimization 57 (2018) 1905–1918.
[14] N. Gilmore, V. Timchenko, C. Menictas, Manifold microchannel heat sink topology optimization, International Journal of Heat and Mass Transfer 170 (2021) 121025.
[15] Y. Zhou, T. Nomura, E.M. Dede, Topology optimization of manifold microchannel heat sinks, in: 2020 19thIEEE Intersociety Conference on Thermal and Thermomechanical Phenomena in Electronic Systems, 2020, pp. 740–746.
[16] S. Sun, P. Liebersbach, X. Qian, 3D topology optimization of heat sinks for liquid cooling, Applied Thermal Engineering 178 (2020) 115540.
[17] E.M. Dede, S.N. Joshi, F. Zhou, Topology optimization, additive layer manufacturing, and experimental testing of an air-cooled heat sink, Journal of Mechanical Design 137 (11) (2015) 111403.
[18] X. Han, H. Liu, G. Xie, L. Sang, J. Zhou, Topology optimization for spider web heat sinks for electronic cooling, Applied Thermal Engineering 195 (2021) 117154.
[19] S.N. Joshi, Z. Yu, H. Sennoun, J. Hampshire, E.M. Dede, Single-phase cooling performance of a topology optimized and additively-manufactured multi-pass branching microchannel heat sink, in: 2020 19th IEEE Intersociety Conference on Thermal and Thermomechanical Phenomena in Electronic Systems, 2020, pp. 790–795.
[20] B.S. Lazarov, O. Sigmund, K.E. Meyer, J. Alexandersen, Experimental validation of additively manufactured optimized shapes for passive cooling, Applied Energy 226 (2018) 330–339.
[21] S. Ozguc, L. Pan, J.A. Weibel, Topology optimization of microchannel heat sinks using a homogenization approach, International Journal of Heat and Mass Transfer 169 (2021) 120896.
[22] "Material Data Sheet – AlSi10Mg-0403 powder for additive manufacturing," https://resources.renishaw.com.
[23] F.P. Incropera, D.P. DeWitt, T.L. Bergman, A.S. Lavine, Fundamentals of Heat and Mass Transfer, Wiley, (2011).
[24] O. Sigmund, Morphology-based black and white filters for topology optimization, Structural and Multidisciplinary Optimization 33 (2007) 401–424.
[25] T.V. Oevelen, Ph.D. dissertation, Katholieke Universiteit Leuven, Leuven, Belgium, 2014.
[26] D. Givoli, A tutorial on the adjoint method for inverse problems, Computer Methods in Applied Mechanics and Engineering 380 (2021) 113810.
[27] F. Palacios-Gomez, L. Lasdon, M. Engquist, Nonlinear optimization by successive linear programming, Management Science (pre-1986) 28 (10) (1982) 1106–1120.